PCCP

ROYAL SOCIETY OF CHEMISTRY

PAPER

Cite this: *Phys. Chem. Chem. Phys.*, 2021, **23**, 24200

Understanding the influence of geometric and electronic structure on the excited state dynamical and photoredox properties of perinone chromophores†

Kaylee A. Wells,‡[a] Jonathan R. Palmer, ‡[a] James E. Yarnell, [ab] Sofia Garakyaraghi, [a] Barry C. Pemberton, [ac] Joseph M. Favale,[a] Mary Katharine Valchar,[a] Arnab Chakraborty[a] and Felix N. Castellano *[a]

Received 23rd August 2021,
Accepted 14th October 2021

DOI: 10.1039/d1cp03870b

rsc.li/pccp

In this work, a series of eight similarly structured perinone chromophores were synthesized and photophysically characterized to elucidate the electronic and structural tunability of their excited state properties, including excited state redox potentials and fluorescence lifetimes/quantum yields. Despite their similar structure, these chromophores exhibited a broad range of visible absorption properties, quantum yields, and excited state lifetimes. In conjunction with static and time-resolved spectroscopies from the ultrafast to nanosecond time regimes, time-dependent computational modeling was used to correlate this behavior to the relationship between non-radiative decay and the energy-gap law. Additionally, the ground and excited state redox potentials were calculated and found to be tunable over a range of 1 V depending on the diamine or anhydride used in their synthesis (E^{red}* = 0.45–1.55 V; E^{ox}* = −0.88 to −1.67 V), which is difficult to achieve with typical photoredox-active transition metal complexes. These diverse chromophores can be easily prepared, and with their range of photophysical tunability, will be valuable for future use in photofunctional applications.

Introduction

Perinone and other polycyclic benzimidazole chromophores have recently emerged as promising molecules in a variety of photofunctional devices and materials. Perinones have already found extensive use in the dye industry,[1,2] and have begun to pique interests for use in many organic electronics.[1,3–5] These newfound interests are due to these chromophores' intense visible light-harvesting capabilities,[1,3–5] significant electron mobilities,[3,4,6] large fluorescence quantum yields,[1,3,5] and exceptional photochemical and thermal stabilities.[1,2,7] Characteristics of perinone photophysics are similar to analogous perylene and naphthalene diimide derivatives, which have already found use in chemical sensing,[8–10] organic field effect transistors,[11–14] light-emitting diodes,[15–17] and photovoltaics.[12,18–21] Additionally, perinones have recently been investigated as cyclometalating and chelating diimine ligands in iridium(III)[22] and rhenium(I)[23] transition metal complexes, respectively, resulting in some of the first reported cases of easily accessing the long-lived triplet manifold of perinone chromophores *via* the heavy-atom effect. More recently, accessing the triplet state of perinones without the use of a transition metal has been investigated by our laboratory by substituting the C=O with a C=S moiety.[24] Ultimately, these investigations have opened up doors for the general perinone framework to be used in a variety of applications where energy can be extracted from a long-lived triplet excited state *via* triplet–triplet energy transfer (TTET).[25]

The basic perinone scaffold is most easily synthesized *via* solid-state sublimation/direct condensation of diamine and anhydride starting materials, as demonstrated by Anzenbacher and coworkers.[5] This "green" synthetic method exhibits simplicity and limited material and purification costs, while still being able to access diverse perinone architectures. For example, Anzenbacher and coworkers were able to use this method to synthesize 48 different perinone analogs in high yield and study their basic photophysical properties.[3] They found that this class of molecule was easily tuned across the entire visible spectrum to desired absorption and emission maxima depending on the nature of the diamine or anhydride used in the synthesis. In addition to basic optical studies,

[a] *Department of Chemistry, North Carolina State University, Raleigh, North Carolina, 27695-8204, USA. E-mail: fncastel@ncsu.edu*
[b] *Department of Chemistry & Chemistry Research Center, United States Air Force Academy, Colorado Springs, Colorado, 80840-6230, USA*
[c] *School of Natural Sciences and Mathematics, Stockton University, Galloway, 08205, USA*

† Electronic supplementary information (ESI) available. See DOI: 10.1039/d1cp03870b

‡ These authors contributed equally.

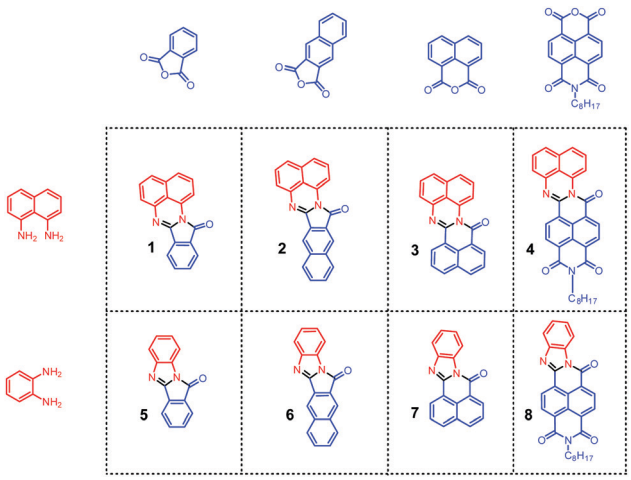

Fig. 1 Structures of the molecules investigated in this study.

electrochemical characterization of their ground state redox potentials was used to estimate how the HOMO–LUMO energies change across the series. However, in-depth investigations correlating observed photophysical properties to underlying electronic and geometric structures have yet to be conducted for this class of photostable dye, preventing the photophysical tunability of this system from being fully realized.

In this work, the static and time-resolved photophysical properties of a series of perinone chromophores were rigorously investigated *via* spectroscopic, electrochemical, and computational methods. Some of the chromophores presented in this study (Fig. 1) have been synthesized previously (**1–3**, **5**, and **7**) and others are new to the literature (**4**, **6**, and **8**). All molecules in the study exhibited strong charge transfer character in their lowest energy singlet excited state, resulting in significant solvatochromism in their absorption and emission spectra. Following excitation into the first singlet excited state, ultrafast transient absorption experiments confirmed no other excited state was populated. Despite the similar structures, computational modeling revealed differences in the degree of excited state distortion upon excitation into the lowest singlet state. Ultimately, this phenomenon aided in modulating the fluorescence decay of each chromophore depending on the degree of excited state distortion. In addition, the decay from the first singlet excited state in these molecules was demonstrated to follow the energy gap law, where the rate constant for non-radiative decay varied over 4 orders of magnitude while the rate constant for radiative decay remained similar across the series. Finally, electrochemistry experiments in conjunction with optical spectroscopy allowed the elucidation of excited state redox potentials, revealing the ability of perinones to be potent and highly tunable photo-oxidants and reductants.

Experimental

Reagents and chemicals

All reagents were purchased from Sigma-Aldrich or Alfa Aesar and used as received. Chromophores **1–3**, **5**, and **7** were synthesized and purified according to their published procedures, yielding structural characterization data matching previously reported values.[3,5,24] The *N*-octylnaphthalene-1,8-dicarboxylic anhydride-4,5-dicarboximide, used as a precursor for **4** and **8**, was prepared according to literature procedures.[26] The identity and purity of all final products were confirmed using ^{1}H NMR, high-resolution mass spectrometry, and elemental analysis, which are all represented in the ESI.†

Synthesis of 2-octylbenzo[*lmn*]perimidino[2,1-*b*][3,8]phenanthroline-1,3,6(2*H*)-trione (4). Naphthalene-1,8-diamine (0.090 g, 0.568 mmol), *N*-octylnaphthalene-1,8-dicarboxylic anhydride-4,5-dicarboximide (0.204 g, 0.538 mmol), and glacial acetic acid (50 mL) were heated to 145 °C inside a pressure vessel for 24 h. Once cool, the precipitate was collected on a frit and washed with acetic acid and deionized water, and then dried under vacuum for 24 hours. The crude product was sublimed at 400 °C and obtained in 59% yield. ^{1}H NMR (500 MHz, CD_2Cl_2) (Fig. S10–S12, ESI†), δ: MS [HR-ESI (CH_2Cl_2) *m*/*z*] (Fig. S13, ESI†) 502.2126 $[M + H]^+$, calcd ($C_{32}H_{28}N_3O_3$) 502.2131. Elemental analysis for $C_{32}H_{27}N_3O_3$, calculated (found): C, 76.63 (76.46); H, 5.43 (5.28); N, 8.38 (8.36).

Synthesis of 12*H*-benzo[*f*]benzo[4,5]imidazo[2,1-*a*]isoindol-12-one (6). Benzene-1,2-diamine (1.613 g, 10 mmol), 2,3-naphthalenedicarboxylic anhydride (1.613 g, 15 mmol), and glacial acetic acid (50 mL) were heated to 145 °C inside a pressure vessel for 24 h. Once cool, the precipitate was collected on a frit and washed with acetic acid and deionized water, and then dried under vacuum for 24 hours. The crude product was sublimed at 220 °C and obtained in 19% yield.^{1}H NMR (500 MHz, CD_2Cl_2) (Fig. S17 and S18, ESI†), δ: MS [HR-ESI (CH_2Cl_2) *m*/*z*] (Fig. S19, ESI†) 271.0874 $[M + H]^+$, calcd ($C_{18}H_{11}N_2O$) 271.0871. Elemental analysis for $C_{18}H_{10}N_2O{\cdot}0.1AcOH$, calculated (found): C, 79.12 (79.08); H, 3.79 (3.94); N, 10.14 (10.27).

Synthesis of 2-octylbenzo[*lmn*]benzo[4,5]imidazo[2,1-*b*][3,8]phenanthroline-1,3,6(2*H*)-trione (8). Benzene-1,2-diamine (0.252 g, 2.33 mmol), *N*-octylnaphthalene-1,8-dicarboxylic anhydride-4,5-dicarboximide (0.783 g, 2.06 mmol), and glacial acetic acid (25 mL) were heated to 145 °C inside a pressure vessel for 24 h. Once cool, the precipitate was collected on a frit and washed with deionized water, and then dried under vacuum for 24 hours. The crude product was sublimed at 400 °C and obtained in 66% yield. ^{1}H NMR (500 MHz, CD_2Cl_2) (Fig. S23–S25, ESI†), δ: MS [HR-ESI (CH_2Cl_2) *m*/*z*] (Fig. S26, ESI†) 452.1976 $[M + H]^+$, calcd ($C_{28}H_{26}N_3O_3$) 452.1974. Elemental analysis for $C_{28}H_{25}N_3O_3$, calculated (found): C, 74.48 (74.58); H, 5.58 (5.60); N, 9.31 (9.42).

General techniques

^{1}H NMR spectra were recorded on a Bruker Avance NEO 500 MHz NMR. The resulting spectra were processed using the MestReNova 10.0.2 software package, with chemical shifts referenced to residual solvent signals. High resolution electrospray ionization mass spectrometry was measured by the Michigan State University Mass Spectrometry Core, East Lansing, MI. Elemental analysis was performed by Atlantic Microlab, Inc., Norcross, GA. Optical absorption spectra were

measured on a Shimadzu UV-3600 spectrophotometer. Steady-state luminescence spectra were obtained from an Edinburgh FLS 980, equipped with a 450 W Xe arc lamp as the excitation source and a Peltier cooled photomultiplier tube (PMT) (R2658P Hamamatsu). Steady-state photoluminescence of each chromophore was collected following excitation into their lowest energy absorbance maximum. Quantum yield measurements were performed on chromophores **1**/**2**/**8** using degassed $[Ru(bpy)_3](PF_6)_2$ in acetonitrile as a standard (λ_{em} 621 nm, Φ_{PL} = 0.095),[27] chromophore **3** using aerated $[Ru(bpy)_3](PF_6)_2$ in acetonitrile as a standard (λ_{em} 621 nm, Φ_{PL} = 0.018),[27] chromophore **4** using degassed $[Os(phen)_3](PF_6)_2$ in acetonitrile as a standard (λ_{em} 718 nm, Φ_{PL} = 0.030),[28] and chromophores **5–7** using *N*-(4-methylphenyl)-4-(1-piperidinyl)naphthalene-1,8-dicarboximide (PNI-Tol) in toluene as a standard (λ_{em} 500 nm, Φ_{PL} = 0.91).[29] Spectroscopic samples were prepared using spectroscopic grade solvent.

Time-correlated single photon counting (TCSPC)

Time-resolved emission experiments were accomplished using a TCSPC spectrometer (Edinburgh Instruments, Lifespec II) described previously.[30] Briefly, photoluminescence signals were measured using a multichannel plate photomultiplier tube (Hamamatsu R3809U-50) in a Peltier-cooled housing. A Ti:sapphire laser (Chameleon Ultra II, Coherent) was utilized as the excitation source and was tuned between 800–1000 nm, depending on the chromophore. The laser output was pulse-picked to a 4 MHz repetition rate (Coherent 9200 Pulse Picker) and frequency doubled (APE-GmbH SHG Unit) to create excitation wavelengths (λ_{ex} = 400–500 nm). Chromophores **1–4** and **5–8** were excited at 450 and 400 nm, respectively.

Electronic structure theory calculations

Density functional theory (DFT) and time-dependent DFT calculations were performed on all chromophores (**1–8**) using the Gaussian 09 software package (revision D.01)[31] and the computation resources of the North Carolina State University High Performance Computing Center. Geometry optimizations and time-dependent DFT calculations were performed using the M06 functional[32] and the Def-2-TZVP basis set on all atoms.[33,34] The polarizable continuum model (PCM)[35] was used to simulate the effects of the THF solvent environment for all calculations. The GD3 dispersion correction[36] was applied to all optimized structures since it resulted in superior agreement of time-dependent DFT with experimental data. Frequency calculations were performed on all optimized structures and no imaginary frequencies were obtained for any of the optimized geometries. The energy, oscillator strength, and related molecular orbital contributions for the 50 lowest singlet–singlet transitions were obtained from the time-dependent DFT output files. The frontier molecular orbitals were generated and visualized with Gaussview 5.0 (Isovalue = 0.02).[37]

Ultrafast transient absorption (TA) spectroscopy

Sub-picosecond transient absorption measurements were conducted using an amplified Ti:sapphire laser system described previously.[38] Briefly, a portion of the output from a 1 kHz Ti:sapphire Coherent Libra regenerative amplifier (4 mJ, 100 fs (fwhm) at 800 nm) was split into the pump and probe beams. The pump beam was directed into an optical parametric amplifier (Coherent OPerA Solo) to generate the tunable excitation source, while the probe beam was delayed using an optical delay stage (6 ns time window). The probe beam was focused onto a calcium fluoride crystal to generate a while light continuum between 350 to 750 nm. The two beams were spatially and temporally overlapped onto the sample, with the relative polarizations of the pump and probe beams set at the magic angle. Samples were contained in 2 mm path length quartz cuvettes and the solutions were stirred continuously throughout the experiment to prevent local heating and sample decomposition. Ground state electronic absorption spectra were taken before and after each experiment to ensure there was no sample degradation during the experiment. All samples were prepared in spectrophotometric grade solvent and the optical densities of the sample solutions at the excitation wavelength were approximately 0.2–0.8. The pump power at the sample was 0.5 μJ per pulse. Transient kinetics were evaluated using the fitting routines available in Origin 2018b (9.55).

Electrochemistry

Differential-pulse voltammetry (DPV) measurements were performed using CH Instruments model 600E series potentiostat. The measurements were carried out under an inert and dry atmosphere of nitrogen in a glovebox (MBraun). Oxidation and reduction potentials were recorded in spectroscopic grade acetonitrile containing 0.1 M tetrabutylammonium hexafluorophosphate ($TBAPF_6$) as the supporting electrolyte. A platinum disk was used as the working electrode (1.6 mm), a platinum wire as the counter electrode, and Ag/$AgNO_3$ as the reference electrode. Each measurement was calibrated using ferrocenium/ferrocene (Fc^+/Fc) as a standard.

Results and discussion

Synthesis

Chromophores **1**, **3**, **5**, and **7** were synthesized using a one-step procedure originally reported by Anzenbacher and coworkers,[3,5] with the resulting structures shown in Fig. 1. For the one-step procedure, the anhydride (1 eq.), diamine (1 eq.), and catalytic zinc acetate (10 mol %) were ground together and heated for prolonged periods in test tubes, resulting in a stark visible colour change to the solid mixture in each case. Once cooled to room temperature, the entire crude product was then purified *via* silica plug and recrystallization. Chromophore **2** was synthesized following a slightly modified version of the procedure established by Anzenbacher and coworkers, but was first presented by our laboratory.[24] Chromophores **4**, **6**, and **8** were synthesized by adding the anhydride (1 eq.) and the diamine (1 eq.) to glacial acetic acid in a pressure vessel and heating to 145 °C for 24 hours. The solids were filtered and washed with acetic acid and water. Finally, all eight chromophores were further purified by sublimation then characterized by ^{1}H NMR,

high resolution electrospray ionization mass spectrometry, and elemental analysis. Structural characterization data for chromophores **1–3**, **5**, and **7** quantitatively matched previously reported values.[3,5,24]

Electronic structure theory calculations

DFT and TD-DFT calculations were performed to probe the electronic structures of **1–8** and help decipher the character of their low-energy singlet manifolds. The M06-D3/Def-2-TZVP level of theory was found to show the best agreement with the published crystal structure and electronic spectrum of **7** (M06[32] and Def-2-TZVP[33,34]). This methodology has also been previously successful in modelling a series of related perinone architectures featuring a thionated carbonyl group.[24]

The optimized ground state structures of all eight chromophores were first calculated in THF as the solvent. The optimized structures of each chromophore in the lowest-energy singlet excited-state (S_1) were then calculated under the same conditions using TD-DFT. These geometries were analysed and compared to the ground state structures to understand the structural evolution of chromophores **1–8** upon excitation into their low-energy singlet manifold and facilitate discussion of the ensuing photophysical processes. The optimized structures of chromophores **3** and **7** in both the ground state and first singlet excited state are shown in Fig. 2 and serve as representative examples of the two types of geometries observed for these chromophores. For chromophore **7**, both the ground and excited-state geometries were found to be planar, revealing the significant rigidity of this chromophore upon photoexcitation. The ground-state geometry of **3** exhibits substantial dihedral angles (11–24°) in its core ring system, adopting a propeller-like geometry. In the excited-state, these dihedral angles distort towards planarity (4–19°), exhibiting much less rigidity than **7**. The same behaviour is observed for chromophore **4**, while the remaining chromophores are planar in both the ground and excited states. This data is summarized in Table 1.

Using the same level of theory, the frontier molecular orbitals of each chromophore were calculated from the optimized ground state geometries (Fig. S27 and S28, ESI†). The highest occupied molecular orbital (HOMO) and lowest unoccupied molecular orbital (LUMO) of each chromophore

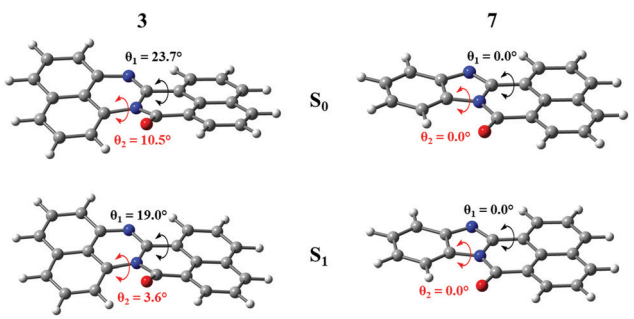

Fig. 2 Optimized geometries of S_0 (top) and S_1 (bottom) of **3** (left) and **7** (right). Geometry optimizations performed at M06-D3/Def2-TZVP level of theory.

Table 1 Core dihedral angles of optimized S_0 and S_1 structures

Molecule	Optimized S_0 θ_1 (°)	Optimized S_1 θ_1 (°)	Optimized S_0 θ_2 (°)	Optimized S_1 θ_2 (°)
1	0.00	0.00	0.00	0.00
2	0.00	0.00	0.00	0.00
3	−23.72	−19.04	−10.54	−3.61
4	−22.24	−20.36	−9.77	−4.69
5	0.00	0.00	0.00	0.00
6	0.00	0.00	0.00	0.00
7	0.00	0.00	0.00	0.00
8	0.00	0.00	0.00	0.00

are presented in Fig. 3. Throughout the series, the frontier orbitals show the HOMO and LUMO to be π and π* in character, respectively. The HOMO of each chromophore displays a significant amount of electron density centred on the diamino moiety, while the LUMO displays much more electron density centred on the anhydride moiety, suggesting charge-transfer (CT) character in the lowest energy transition of each chromophore. The remainder of the frontier orbitals in these chromophores also exhibit significant π (HOMO−1, HOMO−2) or π* (LUMO+1) character. Accordingly, it is expected that the low-energy singlet manifold of each chromophore is dominated by intense π → π* transitions. To further support these predictions, the transitions between the frontier orbitals of **1–8** were calculated *via* TD-DFT and are reported in Table S2 (ESI†) for the two lowest-lying singlet–singlet transitions. In all eight molecules, the lowest-lying transition ($S_0 \rightarrow S_1$) exhibits moderate to high oscillator strength and corresponds to the primarily HOMO–LUMO π → π* transition. The $S_0 \rightarrow S_2$ transition varies much more across the series and includes contributions from many different frontier orbitals. However, these transitions are still primarily π → π*, but with much less CT character.

Steady-state spectroscopy

The electronic absorption spectra of chromophores **1–8** measured in THF are shown in Fig. 4, with other relevant data reported in Table 2. The lowest energy absorption band of each chromophore is consistent with the moderately intense π → π* transitions with varying degrees of CT character predicted by TD-DFT analysis. Chromophores **1** and **2** have significant vibronic structure with maximum absorbance values at 446 and 438 nm, respectively, suggesting a more localized π → π* transition. In contrast, the lowest energy absorbance bands for chromophores **3–8** are broad and featureless, indicating substantial CT character. All eight chromophores possess moderately intense low energy transitions with molar extinction coefficients ranging from 4200 to 14 900 M^{-1} cm^{-1}. The low energy transitions follow the general rule of "particle in a box," where increased conjugation leads to a lower energy π → π* transition. One outlier of this trend worth noting is the blue-shift of the low energy transition when adding an additional aromatic ring to the phenyl anhydride moiety (chromophore **1** *vs.* **2**). This result agrees with the larger energy gap between the HOMO and LUMO calculated for chromophore **2**, as presented in Fig. 3. Energies of the HOMO/LUMO and other select frontier

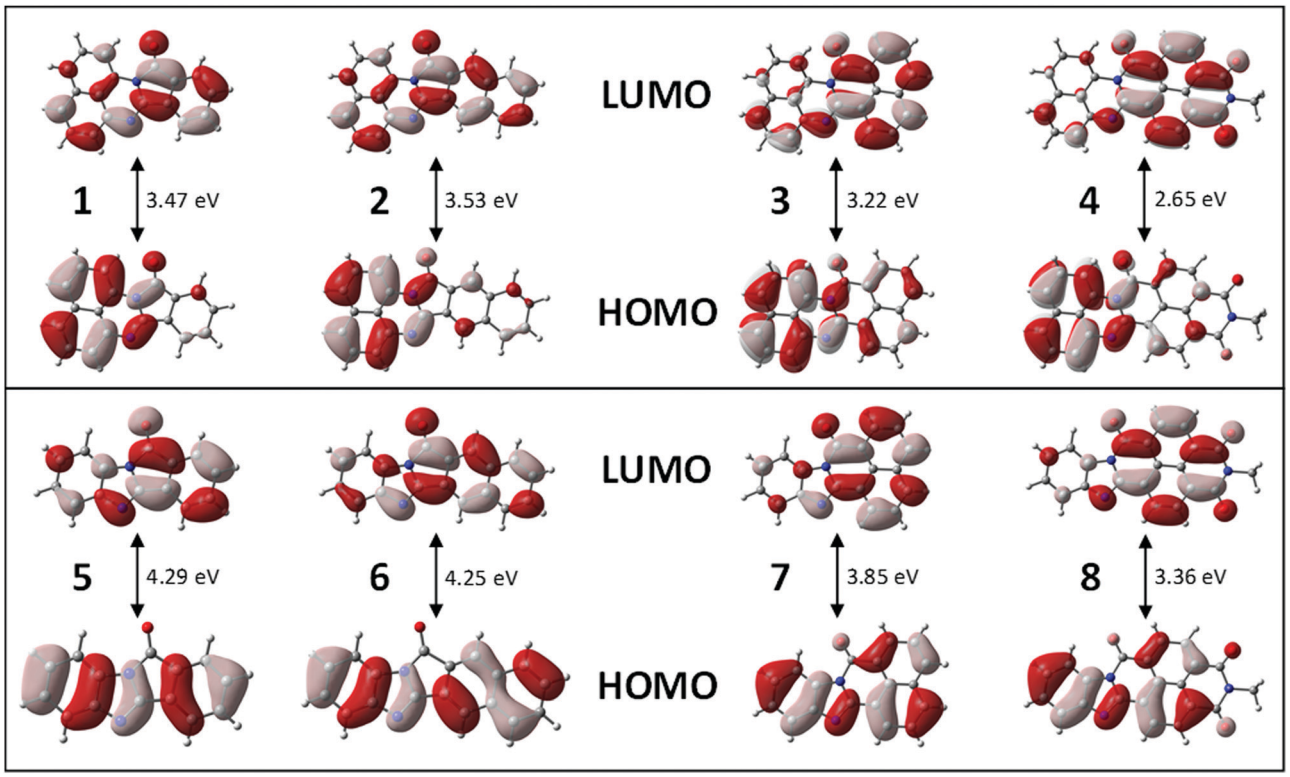

Fig. 3 Pictorial representations of highest occupied and lowest unoccupied molecular orbitals for **1–8**. Calculations performed at M06-D3/Def2-TZVP level of theory with PCM correction.

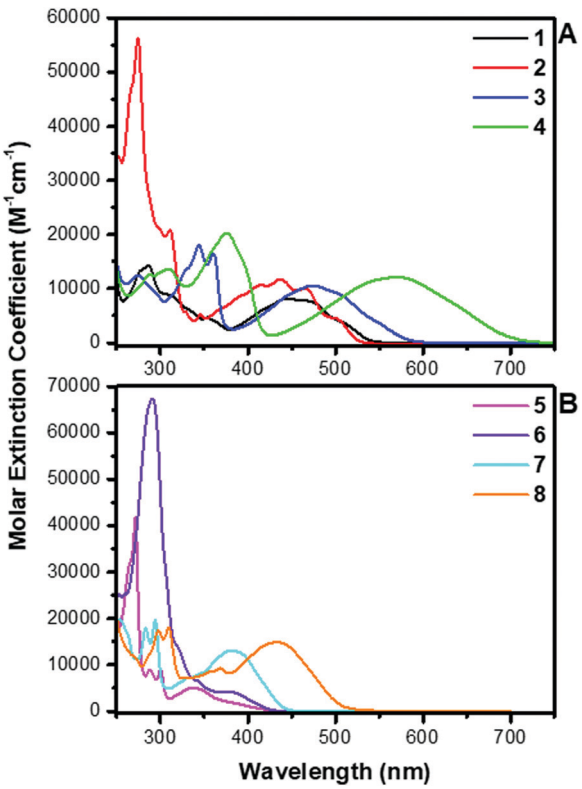

Fig. 4 Electronic spectra of **1–4** (A) and **5–8** (B) in THF.

molecular orbitals calculated at the M06-D3/Def2-TZVP level of theory are also reported in Table S1 (ESI†) for each chromophore.

The photoluminescence spectra of chromophores **1–8** are shown in Fig. 5. The observed photoluminescence is attributed to fluorescence from the initially populated S_1 $\pi \rightarrow \pi^*$ state in each case. As observed with the electronic absorbance spectra, the photoluminescence of chromophores **3–8** have significant CT character (broad and featureless) while **1** and **2** feature structured emission, suggesting a more localized $\pi \rightarrow \pi^*$ emissive event. However, all chromophores exhibit positive solvatochromism and increasing Stokes shifts when dissolved in solvents of increasing polarity, exhibiting classic CT behaviour (Fig. S29–S36 and Table S3, ESI†).[29,39,40] Upon cooling to 77 K in 2-methyl-THF, the fluorescence of all chromophores blue-shifts relative to 298 K emission in THF with the vibronic structure becoming more defined (Fig. S37, ESI†). The observed thermally-induced Stokes shifts (318–1483 cm^{-1}) are further support of CT character since the surrounding solvent shell cannot effectively reorganize to stabilize the expected large excited-state dipoles in these chromophores.[41] These shifts are much larger than the <200 cm^{-1} blue-shifts expected for the non-polar, localized $\pi \rightarrow \pi^*$ states of typical organic chromophores.[42]

Electrochemistry

The oxidation and reduction potentials of all chromophores were determined *via* DPV in acetonitrile and are summarized in Table 2 (Fig. S38 and S39, ESI†). While some molecules

Table 2 Steady-state photophysical and electrochemical data of the chromophores in this study[a]

Molecule	$\lambda_{abs\,max}$ (nm) (ε, M^{-1} cm^{-1})[b]	$\lambda_{em\,max}$ (nm) (298 K)	$\lambda_{em\,max}$ (nm) (77 K)	$\Delta E_{77-298\,K}$[c] (cm^{-1})	E^{red}[d] (V)	E^{ox}[d] (V)	E^{red*}[e] (V)	E^{ox*}[e] (V)
1	286 (14 300), 446 (8200)	598	576	639	−1.68	0.74	0.65	−1.59
2	274 (56 300), 438 (11 700)	574	560	436	−1.71	0.73	0.69	−1.67
3	344 (18 000), 361 (16 500), 474 (10 500)	666	635	733	−1.67	0.66	0.45	−1.46
4	375 (20 200), 570 (12 100)	782	763	318	−1.00	0.72	0.75	−1.03
5	271 (41 700), 336 (5000)	519	497	853	−1.68	1.55	0.92	−1.05
6	291 (67300), 377 (4200)	486	460	1163	−1.72	1.42	1.14	−1.44
7	283 (17 800), 294 (19 800), 380 (13 100)	494	472	944	−1.58	1.30	1.21	−1.49
8	298 (17 400), 310 (18 100), 432 (14 900)	587	540	1483	−0.89	1.56	1.55	−0.88

[a] Measurements were taken using THF as a solvent. [b] Molar extinction coefficients determined for the lowest energy transition at $\lambda_{abs\,max}$. [c] Thermally induced Stokes shift determined by taking the difference in energy between room temperature and 77 K emission maxima. [d] Ground state redox potentials determined by differential pulse voltammetry in 0.1 M solution of Bu_4NPF_6 in ACN *vs.* Fc/Fc^+. [e] $E^{red*} = E^{red} + E_{00}$ and $E^{ox*} = E^{ox} - E_{00}$ where E_{00} was taken from the highest energy vibronic feature of the emission spectrum at 77 K in 2-MeTHF (Fig. S37, ESI).

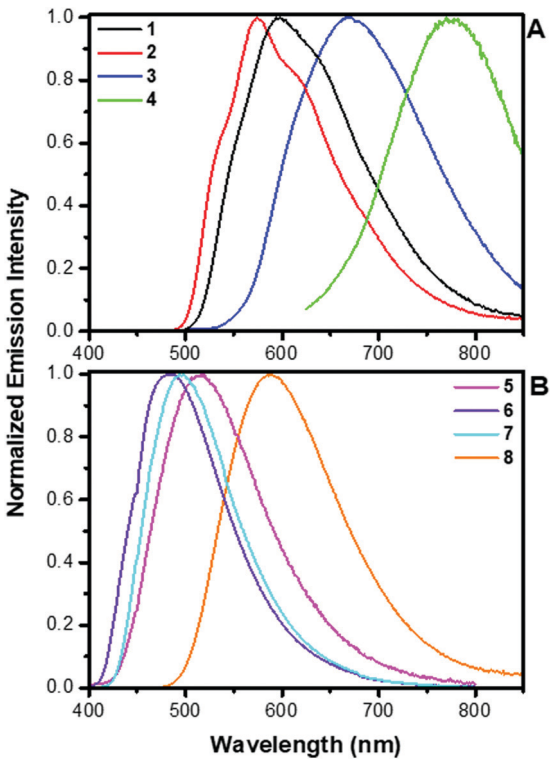

Fig. 5 Photoluminescence spectra of **1–4** (A) and **5–8** (B) in aerated THF.

displayed multiple oxidation and reduction peaks, only the first oxidation and reduction potentials were considered in the analysis of these chromophores. The oxidation potentials of each chromophore correlate well with respect to the diamine that was used in its synthesis. Chromophores **1–4**, which are synthesized from the 1,8-diaminonapthalene, have similar oxidation potentials that range from 0.66 to 0.74 V. The oxidation potentials of chromophores **5–8**, which are synthesized from the *o*-phenelynediamine, are notably more positive and range from 1.30 to 1.56 V. As with the shared diamine starting material, the chromophores that share the same anhydride starting material (*i.e.* **1** and **5**, **2** and **6**, **3** and **7**, and **4** and **8**) have either identical or similar reduction potentials, *e.g.* −1.68 V for chromophores **1** and **5**. It should also be noted that the first oxidation and reduction potentials of chromophores **1**, **3**, **5**, and **7** have previously been analysed in dichloromethane.[3] The energy gaps between the first oxidation and reduction potentials of these chromophores found in the previous study are in agreement with the energy gaps found in this study, where the electrochemistry was carried out in acetonitrile.

From the ground state redox potentials, the oxidation and reduction potentials of the first singlet excited state were also estimated for each of these chromophores using $E^{red*} = E^{red} + E_{00}$ and $E^{ox*} = E^{ox} - E_{00}$,[43] where E_{00} was taken from the highest energy vibronic feature of the emission spectrum measured at 77 K in 2-MeTHF (Fig. S37, ESI†). The resultant values are given in Table 2. The excited state reduction potentials (E^{red*}) of all eight chromophores are positive in magnitude and span a range of values from 0.45–1.55 V, illustrating a large tunability in the excited state reduction potential depending on the chromophore. Of particular note, chromophore **8** has significant promise as a potent photo-oxidant, with an E^{red*} of 1.55 V. Conversely, the excited state oxidation potentials of all eight chromophores were negative in magnitude and the range of values varied much less across the series (−0.88 to −1.67 V). In this case, chromophore **2** is estimated to be the most potent photo-reductant, with an E^{ox*} of −1.67 V.

Radiative and non-radiative decay rates

The quantum yields (Φ_f) and lifetimes (τ_f) of fluorescence for chromophores **1–8** are reported in Table 3. Although similarly structured, the relative fluorescence intensities of chromophores **1–8** in THF drastically vary throughout the series, with quantum yields of fluorescence ranging from <0.0001 for chromophore **4** to 0.71 for chromophore **7**. Additionally, the excited-state lifetimes were adequately fit to single exponential decays and exhibit a similar drastic range of values (11 ps to 11.5 ns, Fig. S40–S46, ESI†). In order to understand this behaviour, the radiative (k_r) and non-radiative (k_{nr}) rates of deactivation were calculated for the emissive state in each chromophore, as summarized in Table 3. Throughout the series, the radiative rate remains relatively constant at values of $\sim 10^7$ s^{-1}, which is indicative of emission originating from states of similar CT character. However, the non-radiative rate varies substantially, ranging four orders of magnitude

Table 3 Radiative and non-radiative decay rates of the chromophores in this study[a]

Molecule	Φ_f (298 K)	τ_f (298 K)	τ_f (77 K)[b]	k_r ($\times 10^7$ s^{-1})	k_{nr} ($\times 10^7$ s^{-1})
1	0.028[c]	871 ps[b]	1.83 ns	3.21	112
2	0.056[c]	1.31 ns[b]	2.55 ns	4.27	72.1
3	0.0014[e]	74 ps[b]	179 ps	1.89	1350
4	<0.0001[f]	11 ps[d]	173 ps	0.79	9090
5	0.062[g]	3.98 ns[b]	13.9 ns	1.56	23.6
6	0.24[g]	9.11 ns[b]	14.1 ns	2.63	8.34
7	0.71[g]	11.5 ns[b]	8.12 ns	6.17	2.52
8	0.17[c]	3.23 ns[b]	7.88 ns	5.26	25.7

[a] Measurements taken using THF as a solvent. [b] Excited state lifetime taken with Edinburgh Lifespec II (TCSPC). [c] Quantum yields measured using deaerated $[Ru(bpy)_3](PF_6)_2$ in acetonitrile as the standard (λ_{em} 621 nm, Φ_{PL} = 0.095). [d] Excited state lifetime determined using ultrafast transient absorption spectroscopy. [e] Quantum yield measured using aerated $[Ru(bpy)_3](PF_6)_2$ in acetonitrile as the standard (λ_{em} 621 nm, Φ_{PL} = 0.018). [f] Quantum yield measured using deaerated $[Os(phen)_3](PF_6)_2$ in acetonitrile as the standard (λ_{em} 718 nm, Φ_{PL} = 0.030). [g] Quantum yield was measured using PNI-Tol in toluene as the standard (λ_{em} 500 nm, Φ_{PL} = 0.91).

(10^7–10^{10} s^{-1}). The observed trend in non-radiative decay rates may best be approximated by the energy-gap-law, as expanded extensively by Meyer and coworkers to CT excited-states.[44–46] In these chromophores, the CT state becomes closer in energetic proximity to the ground-state potential energy surface with decreasing emission energy (*i.e.* chromophore **7** *vs.* **4**), resulting in an increase in the Franck–Condon overlap and hence the enhancement of radiationless deactivation. Fig. 6 presents the linear relationship between the optical emission energy and the natural logarithm of the non-radiative decay rate ($\ln k_{nr}$), with only minor deviations from linearity. It is likely that the significant structural distortion chromophores **3** and **4** experience upon photoexcitation also manifests in the non-radiative deactivation of the excited-state, explaining why they are notably less emissive than the rigid chromophores (**1**, **2**, **5–8**).

Transient absorption spectroscopy

Ultrafast transient absorption spectroscopy was performed on chromophores **1–8** to confirm the photophysical processes that take place after the formation of the initially populated excited state in THF (Fig. 7 and Fig. S48, ESI†). In all instances, single-wavelength kinetic analysis was performed and could be fit to biexponential functions. The excited state features are assigned to vibrational cooling and transitions of the singlet CT state ($S_1 \rightarrow S_0$), where the final observed time-constant corresponds to the decay back down to the ground-state. However, for chromophores **1**, **2**, and **5–8**, the final time-component was not in agreement with the fluorescence lifetime (Table 4). With the introduction of an intermediate time constant and fit to a triexponential decay, the final time constant elongates and becomes in adequate agreement with the fluorescence lifetime. Assignment of the intermediate time constant could not be made due to the lack of a unique spectroscopic feature and exists solely to allow the final time constant to equal the fluorescence lifetime. It is possible that due to the large excited-state dipoles exhibited by these chromophores, the intermediate time constant may arise from the solvent shell reorganizing around the excited state species after relaxing from the initially populated Franck–Condon state. Once the vibrationally cooled excited state is formed, all molecules decay symmetrically down to the ground state.

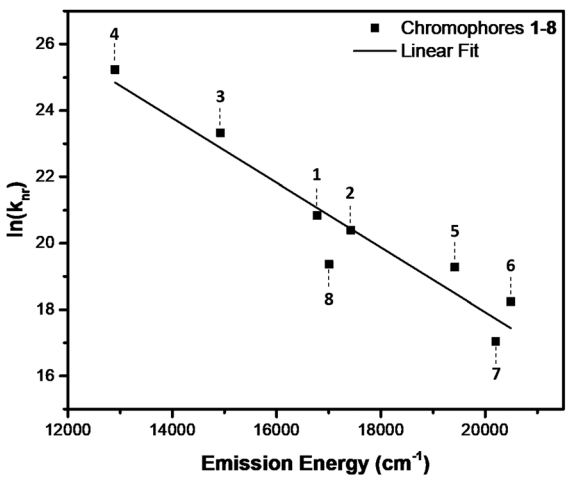

Fig. 6 Energy-gap law plot of chromophores **1–8**.

Upon 495 nm excitation, chromophores **1** and **2**, and 400 nm excitation, **5–7**, (Fig. 7 and Fig. S48, ESI†) decay in a triexponential fashion. The first time-constant is representative of vibrational cooling with sub-picosecond time constants. The latter two time constants are in the tens of ps range for the shorter and the longer time constant approaches that of the molecule's fluorescence lifetime (Tables 3 and 4). The final time constant represents the decay of the singlet excited state back to the ground state. Chromophore **1** has excited state features spanning from 350 to 600 nm peaking at 359, 459, and 555 nm. An isosbestic point lies at 608 nm where the excited state difference spectra transitions from excited state features to stimulated emission that spans out to 750 nm. Chromophore **2** behaves similarly with excited state features centred at 360 and *ca.* 500 nm. However, its isosbestic point is red-shifted slightly at 629 nm. Showing slightly different behaviour *ca.* 750 nm when compared to chromophore **1**, chromophore **2** transitions from stimulated emission into a small excited state feature.

Unlike any of the other chromophores in this study, **5** and **6** exhibit excited state features across the entire visible window probed in this study (Fig. S48, ESI†). No ground state bleaches or stimulated emission features were found, indicating that the excited state of both compounds absorbs more across the visible range than its ground state. Chromophore **5** has excited state features centered at 498 nm and 623 nm. Chromophore **6** exhibits excited state features centred at 350, 422, and 479 nm with a broad feature that begins around 550 nm and extends to the NIR. Chromophore **7** (Fig. 7) exhibits both a ground state bleach prior to 400 nm and a stimulated emission feature between 525 and 595 nm. It exhibits excited state features on either side of the stimulated emission peak at 460 and 712 nm. Single wavelength analysis of these three chromophores yields a trend where the first time constant is short (sub-picosecond

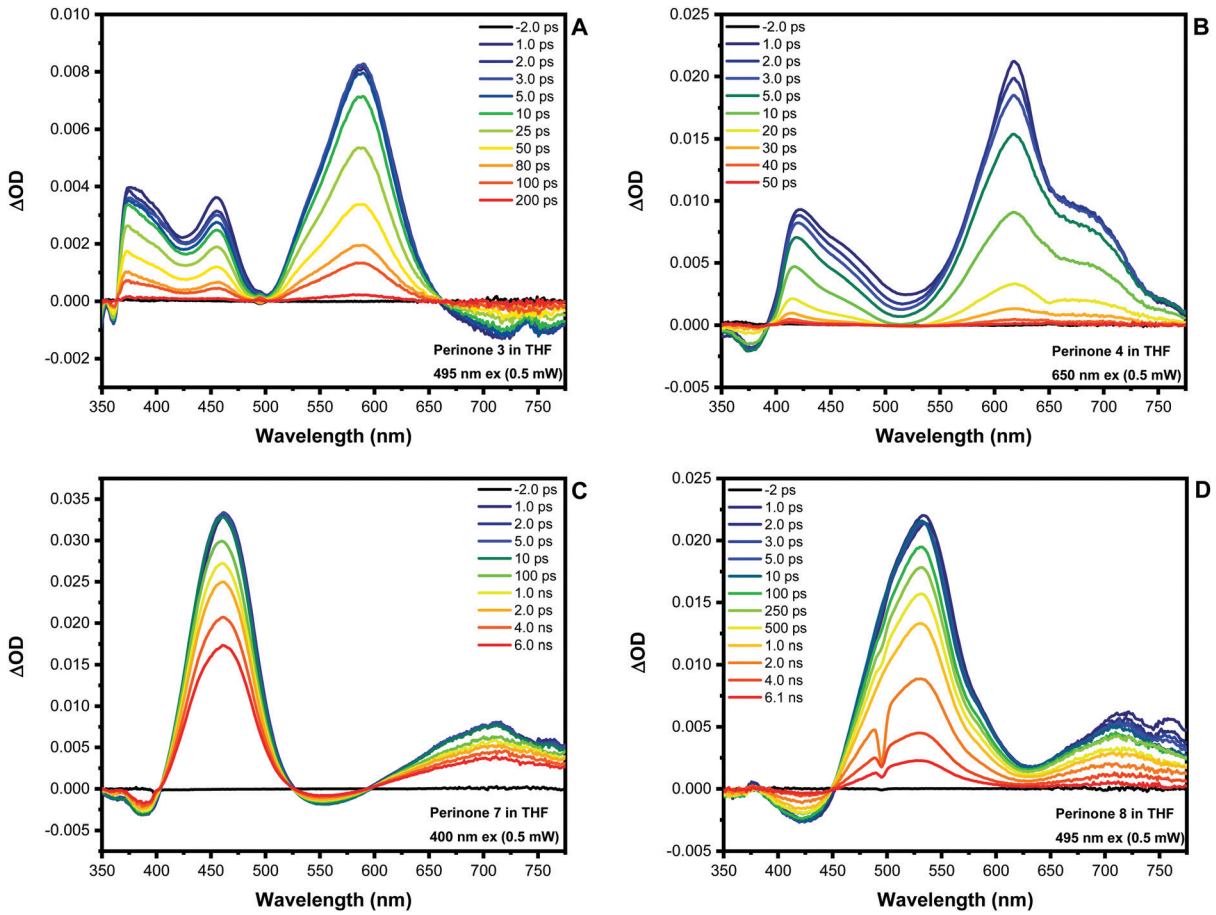

Fig. 7 Excited-state difference spectra of **3** (A) in THF following 495 nm pulsed excitation, **4** (B) in THF following 650 nm pulsed excitation, **7** (C) in THF following 400 nm pulsed excitation, and **8** (D) in THF following 495 nm pulsed excitation (105 fs fwhm).

Table 4 Transient absorption multiple wavelength kinetic analysis

Molecule	τ_1 (ps)	τ_2 (ps)	τ_3 (ns)
1	0.7	53	0.79
2	0.16	48	1.16
3	0.66	52	—
4	0.13	10.8	—
5	0.54	28.4	3.7
6	0.58	43	8.7
7	1.0	33	11
8	1.3	165	2.7

to 1 ps, Table 4) representing vibrational cooling and the latter two are longer in the tens of ps and finally out to the ns domain matching their fluorescence decay (Table 3).

Molecule **8** (Fig. 7) follows a similar kinetic trend after 495 nm excitation in which the first time-constant is of the molecule vibrationally cooling. Unlike the above stated chromophores, chromophore **8** has a second time constant that is hundreds of ps. The third time constant agrees with its photoluminescence lifetime and corresponds to the ground state recovery. Compound **8** has ground state bleaches prior to its isosbestic point at 448 nm. After that point the excited state difference spectrum entails excited state features beyond 750 nm with peaks at 532 (shoulder *ca.* 500 and 585 nm) and 712 nm.

Chromophores **3** (495 nm excitation) and **4** (650 nm excitation) (Fig. 7), relax back to the ground state after being populated into their singlet manifold with a biexponential decay. The first-time constant correlates to vibrational cooling and the second is the recovery of the ground state. We postulate that the significantly shorter lifetimes of these two chromophores is the reason that single-wavelength analysis of their respective excited state species is biexponential in nature and not triexponential as the other chromophores in this series. The excited state difference spectra of **3** is predominantly excited state features with peak maxima at 375, 455, and 590 nm. Chromophore **3** also has two isosbestic points at 364 and 662 nm. Prior to 364 nm, are two ground state bleaches and after 662 nm is stimulated emission. Chromophore **4** is also predominantly characterized by its excited state features centred at 421 (shoulder *ca.* 468 nm) and 620 (shoulder *ca.* 688 nm) nm. Unlike **3**, chromophore **4** exhibits only one isosbestic point at 393 nm, with no stimulated emission observed within the spectral window. Prior to the isosbestic point in chromophore **4** is a ground state bleach and has excited state features centred at 418 and 617 nm (shoulder *ca.* 695 nm).

Solvent effects

Solvatochromic studies were performed to quantify the degree of CT in the lowest energy singlet excited-state of these chromophores. The change in dipole moment between the ground and emissive excited-state may be approximated by the Onsager reaction field model[47] as developed extensively by Lippert[48] and Mataga.[49] Assuming a point dipole placed at the centre of a vacuum cavity in a uniform dielectric continuum, the effects of solvent on the Stokes shift can be expressed in eqn (1) as:

$$\tilde{\nu}_{abs} - \tilde{\nu}_{fl} = \frac{2\Delta f(\mu_e - \mu_g)^2}{hca_0^3} + (\tilde{\nu}_{abs}^{vac} - \tilde{\nu}_{fl}^{vac}) \quad (1)$$

where $\tilde{\nu}_{abs}$ and $\tilde{\nu}_{fl}$ are the energies (cm^{-1}) of absorption and emission maxima for the S_0–S_1 transition, respectively; $\tilde{\nu}_{abs}^{vac}$ and $\tilde{\nu}_{fl}^{vac}$ are the maxima extrapolated to the gas-phase; μ_g and μ_e (esu cm) are the ground and excited-state dipoles, respectively; a_0^3 is the Onsager cavity volume (cm^3),[47] h is the Planck constant (erg s), c is the speed of light (cm s^{-1}), and Δf is the orientation polarizability factor. The orientation polarizability of a medium is defined in eqn (2), where ε is the static dielectric constant and n is the refractive index of the solvent.

$$\Delta f = \frac{\varepsilon - 1}{2\varepsilon + 1} - \frac{n^2 - 1}{2n^2 + 1} \quad (2)$$

The values of Δf for each solvent used in this study are listed in Table S3 (ESI†). It should be noted that eqn (1) best approximates solvatochromic effects on chromophores whose dipole moments in the equilibrium ground and excited-states are oriented relatively parallel (or anti-parallel), such as linear push–pull dyes.[29,50–53] As a result, slight deviations from Lippert–Mataga behaviour are expected for perinones since they are not as straight-forward as typical linear push–pull dyes. The Stokes shifts of **1–8** as a function of the solvent orientation polarizability are plotted in Fig. 8, which present a general linear dependence in the case of each chromophore.

The change in dipole moments ($\mu_e - \mu_g$) were calculated from the slopes of the Lippert–Mataga plots, as shown in Table 5. The Onsager cavity volumes were calculated from the optimized ground-state geometries using the PCM solvation model (M06-D3/Def-2-TZVP). In the case of chromophores **4** and **8**, the *n*-octyl group on the imide nitrogen was substituted with a methyl group for the calculations, as the resulting volume is a better approximation to the effective solvation cavity occupied by the dipole moment.[54] The calculated change in dipole moments vary throughout the series and are relatively large, indicating that significant electronic redistribution occurs upon photoexcitation. Additionally, the increase in Stokes shift for each chromophore with increasing solvent polarity indicates that solvent reorganization likely precedes emission to stabilize the large excited-state dipoles. These observations are consistent with the CT character observed in the electronic structure theory calculations. The calculated change in dipoles also correlate relatively well with the degree of CT predicted by the electronic absorption and fluorescence

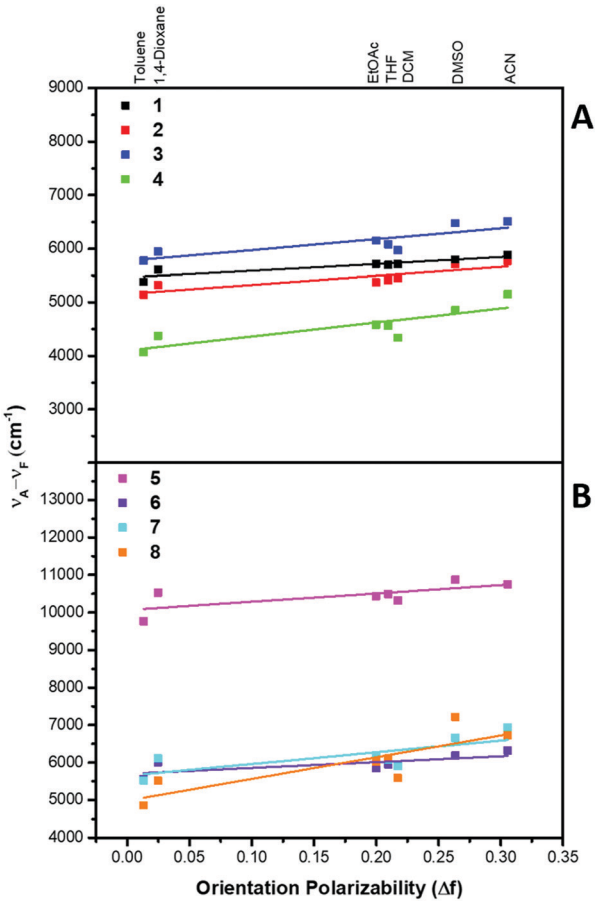

Fig. 8 Lippert–Mataga plots of chromophores **1–4** (A) and **5–8** (B) in aprotic solvents.

Table 5 Change in dipole moment ($\mu_e - \mu_g$) for chromophores **1–8**

Molecule	Cavity volume[a] (10^{-22} cm^3)	Fitted slope[b] (cm^{-1})	$\mu_e - \mu_g$[c] (D)
1	3.46	1270	6.6
2	4.09	1694	8.3
3	4.05	2030	9.0
4	4.82	2612	11.2
5	2.86	2214	7.9
6	3.52	1569	7.4
7	3.44	3134	10.3
8	4.25	5793	15.6

[a] Solvent cavity volumes were obtained from ground state geometry optimizations (M06-D3/Def2-TZVP) using the PCM solvation model. [b] Slopes were obtained from linear regressions on the plots in Fig. 8. [c] Change in dipole moment was calculated using eqn (1).

spectra, where chromophores **1** and **2** exhibit more vibronic character on account of the smaller extent of charge-separation ($\Delta\mu$ = 6.6 and 8.3 D, respectively).

Since the Lippert–Mataga model only accounts for general solvent effects, it is likely that deviations from linear behaviour are also present due to the mean solute polarizabilities in the states involved in the transition, as well as any specific solute–solvent interactions. It is also important to note that the calculated apparent Stokes shifts of **5** (10 000–11 000 cm^{-1})

are consistently much higher than those of the other seven chromophores (4000–7000 cm^{-1}). This phenomenon can be explained by the presence of overlapping singlet–singlet transitions in the lowest energy absorbance band of chromophore **5**. In this case, the $S_0 \rightarrow S_1$ transition is masked by the more intense and slightly higher energy $S_0 \rightarrow S_2$ transition (Fig. S47, ESI†), causing a blue-shift in the apparent low-energy absorbance maximum as demonstrated by TD-DFT analysis. However, since the electronic absorbance spectrum of chromophore **5** is relatively insensitive to solvent polarity (see Fig. S33, ESI†), the slope of the Lippert–Mataga plot is independent of $\tilde{\nu}_{abs}$, allowing the calculation of the change in dipole moment from these inflated Stokes shifts.

Conclusions

In this study, we report the synthesis of three new perinone chromophores (**4**, **6**, and **8**) in addition to five other previously reported molecules. We have explored their excited-state evolution from a transient absorption and photoluminescence viewpoint in addition to their ground state properties. Utilizing electronic structure theory calculations and solvatochromism studies, we were successful in assigning the lowest energy electronic transitions of all eight chromophores as $\pi \rightarrow \pi^*$ with some CT character. All molecules exhibited modest molar absorptivity (4200 to 14 900 M^{-1} cm^{-1}) and varying degrees of visible absorption capabilities, with the most red-absorbing molecule, **4**, exhibiting a visible cross section past 570 nm. While chromophores **1** and **2** displayed significant structure in their absorption and photoluminescence bands, all chromophores exhibited positive solvatochromism in solvents of increasing polarity and thermally induced Stokes shifts suggesting that all molecules studied demonstrate some degree of CT character. Close inspection of the fluorescence quantum yields and lifetimes allowed us to extract non-radiative rate constants that indicated k_{nr} as a function of emission energy was best modelled by the energy-gap-law. Transient absorption studies of each chromophore resulted in excited state difference spectra dominated by excited state absorbance features. These features decayed either entirely within the time delay of the experiment (within 6 ns) or just outside the range of detection ($>$12 ns). It is worth noting here that kinetic decay of these chromophores was not as direct as the spectra insinuates. Select chromophores needed an additional, intermediate time constant to allow for final lifetimes to match the fluorescence lifetimes, despite only two spectral features being present across the entire series. Overall, these vibrant and customizable chromophores have easily tuneable photophysical properties, enabling them to serve as scaffolds for further functionalization or as building blocks in future metal–organic supramolecular structures for deterministic photofunctional applications.

Conflicts of interest

There are no conflicts to declare.

Acknowledgements

This work was supported by the was supported by the National Science Foundation (CHE-1955795). J. E. Y. was supported by the Air Force Institute of Technology (AFIT).

References

1 M. G. Debije, P. P. Verbunt, P. J. Nadkarni, S. Velate, K. Bhaumik, S. Nedumbamana, B. C. Rowan, B. S. Richards and T. L. Hoeks, *Appl. Opt.*, 2011, **50**, 163–169.
2 K. Kobrakov, N. Zubkova, G. Stankevich, Y. S. Shestakova, V. Stroganov and O. Adrov, *Fibre Chem.*, 2006, **38**, 183–187.
3 M. Mamada, C. Pérez-Bolívar, D. Kumaki, N. A. Esipenko, S. Tokito and P. Anzenbacher, *Chem. – Eur. J.*, 2014, **20**, 11835–11846.
4 R. Loutfy, A. Hor, P. Kazmaier, R. Burt and G. Hamer, *Dyes Pigm.*, 1991, **15**, 139–156.
5 M. Mamada, C. S. Pérez-Bolívar and P. Anzenbacher Jr, *Org. Lett.*, 2011, **13**, 4882–4885.
6 K. Y. Law, *Chem. Rev.*, 1993, **93**, 449–486.
7 Y. Nagao, *Prog. Org. Coat.*, 1997, **31**, 43–49.
8 L. Zang, R. Liu, M. W. Holman, K. T. Nguyen and D. M. Adams, *J. Am. Chem. Soc.*, 2002, **124**, 10640–10641.
9 W. Wang, W. Wan, H.-H. Zhou, S. Niu and A. D. Li, *J. Am. Chem. Soc.*, 2003, **125**, 5248–5249.
10 A. Kundu, J. Pitchaimani, V. Madhu, P. Sakthivel, R. Ganesamoorthy and S. P. Anthony, *J. Fluoresc.*, 2017, **27**, 491–500.
11 B. A. Jones, M. J. Ahrens, M. H. Yoon, A. Facchetti, T. J. Marks and M. R. Wasielewski, *Angew. Chem.*, 2004, **116**, 6523–6526.
12 X. Zhan, Z. a. Tan, B. Domercq, Z. An, X. Zhang, S. Barlow, Y. Li, D. Zhu, B. Kippelen and S. R. Marder, *J. Am. Chem. Soc.*, 2007, **129**, 7246–7247.
13 A. Babel and S. A. Jenekhe, *J. Am. Chem. Soc.*, 2003, **125**, 13656–13657.
14 R. P. Ortiz, H. Herrera, R. Blanco, H. Huang, A. Facchetti, T. J. Marks, Y. Zheng and J. L. Segura, *J. Am. Chem. Soc.*, 2010, **132**, 8440–8452.
15 W. Zhang, Y. Xu, M. Hanif, S. Zhang, J. Zhou, D. Hu, Z. Xie and Y. Ma, *J. Phys. Chem. C*, 2017, **121**, 23218–23223.
16 H. F. Higginbotham, P. Pander, R. Rybakiewicz, M. K. Etherington, S. Maniam, M. Zagorska, A. Pron, A. P. Monkman and P. Data, *J. Mater. Chem. C*, 2018, **6**, 8219–8225.
17 C. Ego, D. Marsitzky, S. Becker, J. Zhang, A. C. Grimsdale, K. Müllen, J. D. MacKenzie, C. Silva and R. H. Friend, *J. Am. Chem. Soc.*, 2003, **125**, 437–443.
18 C. Li, Z. Liu, J. Schöneboom, F. Eickemeyer, N. G. Pschirer, P. Erk, A. Herrmann and K. Müllen, *J. Mater. Chem.*, 2009, **19**, 5405–5415.
19 C. W. Tang, *Appl. Phys. Lett.*, 1986, **48**, 183–185.
20 J. Xue, S. Uchida, B. P. Rand and S. R. Forrest, *Appl. Phys. Lett.*, 2004, **85**, 5757–5759.

21 M. A. Angadi, D. Gosztola and M. R. Wasielewski, *J. Appl. Phys.*, 1998, **83**, 6187–6189.
22 J. E. Yarnell, P. De La Torre and F. N. Castellano, *Eur. J. Inorg. Chem.*, 2017, 5238–5245.
23 K. A. Wells, J. E. Yarnell, S. Sheykhi, J. Palmer, D. T. Yonemoto, R. Joyce, S. Garakyaraghi and F. N. Castellano, *Dalton Trans.*, 2021, **50**, 13086–13095.
24 J. R. Palmer, K. A. Wells, J. E. Yarnell, J. M. Favale and F. N. Castellano, *J. Phys. Chem. Lett.*, 2020, **11**, 5092–5099.
25 J. Zhao, W. Wu, J. Sun and S. Guo, *Chem. Soc. Rev.*, 2013, **42**, 5323–5351.
26 N. M. Shavaleev, H. Adams, J. Best and J. A. Weinstein, *J. Organomet. Chem.*, 2007, **692**, 921–925.
27 K. Suzuki, A. Kobayashi, S. Kaneko, K. Takehira, T. Yoshihara, H. Ishida, Y. Shiina, S. Oishi and S. Tobita, *Phys. Chem. Chem. Phys.*, 2009, **11**, 9850.
28 F. Deng, J. R. Sommer, M. Myahkostupov, K. S. Schanze and F. N. Castellano, *Chem. Commun.*, 2013, **49**, 7406–7408.
29 S. R. Greenfield, W. A. Svec, D. Gosztola and M. R. Wasielewski, *J. Am. Chem. Soc.*, 1996, **118**, 6767–6777.
30 J. E. Yarnell, J. C. Deaton, C. E. McCusker and F. N. Castellano, *Inorg. Chem.*, 2011, **50**, 7820–7830.
31 M. Frisch, G. Trucks, H. Schlegel, G. Scuseria, M. Robb, J. Cheeseman, G. Scalmani, V. Barone, B. Mennucci, G. Petersson, H. Nakatsuji, *et al.*, *Gaussian 9, Revision D.01*, 2009.
32 Y. Zhao and D. G. Truhlar, *Theor. Chem. Acc.*, 2008, **120**, 215–241.
33 F. Weigend and R. Ahlrichs, *Phys. Chem. Chem. Phys.*, 2005, **7**, 3297–3305.
34 F. Weigend, *Phys. Chem. Chem. Phys.*, 2006, **8**, 1057–1065.
35 M. Cossi, G. Scalmani, N. Rega and V. Barone, *J. Chem. Phys.*, 2002, **117**, 43.
36 S. Grimme, J. Antony, S. Ehrlich and H. Krieg, *J. Chem. Phys.*, 2010, **132**, 154104.
37 R. Dennington, T. Keith and J. Millam, *GaussView, Ver. 5*, 2009.
38 S. Garakyaraghi, E. O. Danilov, C. E. McCusker and F. N. Castellano, *J. Phys. Chem. A*, 2015, **119**, 3181–3193.
39 K. Tominaga, G. C. Walker, W. Jarzeba and P. F. Barbara, *J. Phys. Chem.*, 1991, **95**, 10475–10485.
40 F. Kournoutas, K. Seintis, N. Karakostas, J. Tydlitat, S. Achelle, G. Pistolis, F. Bureš and M. Fakis, *J. Phys. Chem. A*, 2018, 123, 417–428.
41 J. E. Yarnell, P. De La Torre and F. N. Castellano, *Eur. J. Inorg. Chem.*, 2017, 5238–5245.
42 J. E. Yarnell, K. A. Wells, J. R. Palmer, J. M. Breaux and F. N. Castellano, *J. Phys. Chem. B*, 2019, **123**, 7611–7627.
43 N. Armaroli, *Chem. Soc. Rev.*, 2001, **30**, 113–124.
44 J. V. Caspar and T. J. Meyer, *J. Phys. Chem.*, 1983, **87**, 952–957.
45 J. V. Caspar, E. M. Kober, B. P. Sullivan and T. J. Meyer, *J. Am. Chem. Soc.*, 1982, **104**, 630–632.
46 E. M. Kober, J. V. Caspar, R. S. Lumpkin and T. J. Meyer, *J. Phys. Chem.*, 1986, **90**, 3722–3734.
47 L. Onsager, *J. Am. Chem. Soc.*, 1936, **58**, 1486–1493.
48 E. Lippert, *Z. Naturforsch., A: Astrophys., Phys. Phys. Chem.*, 1955, **10**, 541–545.
49 N. Mataga, Y. Kaifu and M. Koizumi, *Bull. Chem. Soc. Jpn.*, 1956, **29**, 465–470.
50 T. Inari, M. Yamano, A. Hirano, K. Sugawa and J. Otsuki, *J. Phys. Chem. A*, 2014, **118**, 5178–5188.
51 Y. Li, M. Zhou, Y. Niu, Q. Guo and A. Xia, *J. Chem. Phys.*, 2015, **143**, 034309.
52 A. K. Pati, M. Mohapatra, P. Ghosh, S. J. Gharpure and A. K. Mishra, *J. Phys. Chem. A*, 2013, **117**, 6548–6560.
53 Y. Yamaguchi, T. Ochi, Y. Matsubara and Z.-I. Yoshida, *J. Phys. Chem. A*, 2015, **119**, 8630–8642.
54 C. Liu, K.-C. Tang, H. Zhang, H.-A. Pan, J. Hua, B. Li and P.-T. Chou, *J. Phys. Chem. A*, 2012, **116**, 12339–12348.

